HHS Public Access

Author manuscript

Cell. Author manuscript; available in PMC 2018 March 09.

Published in final edited form as:

Cell. 2017 March 09; 168(6): 1065–1074.e10. doi:10.1016/j.cell.2017.02.022.

In situ molecular architecture of the *Salmonella* type III secretion machine

Bo Hu[1,4], **Maria Lara-Tejero**[2,4], **Qingke Kong**[3], **Jorge. E. Galán**[2,5,#], and **Jun Liu**[1,#]

[1]Department of Pathology and Laboratory Medicine, University of Texas Medical School at Houston, Houston TX77030

[2]Department of Microbial Pathogenesis, Yale University School of Medicine, New Haven, CT06536

[3]Department of Infectious Diseases, College of Veterinary Medicine, University of Florida, Gainesville, FL32608

Abstract

Type III protein secretion systems have specifically evolved to deliver bacterially encoded proteins into target eukaryotic cells. The core elements of this multi-protein machine are the envelope-associated needle complex, the inner membrane export apparatus, and a large cytoplasmic sorting platform. Here we report a high-resolution *in situ* structure of the *Salmonella* Typhimurium type III secretion machine obtained by high-throughput cryo-electron tomography and sub-tomogram averaging. Through molecular modeling and comparative analysis of machines assembled with protein-tagged components or from different deletion mutants we determined the molecular architecture of the secretion machine *in situ* and localized its structural components. We also show that docking of the sorting platform results in significant conformational changes in the needle complex to provide the symmetry adaptation required for the assembly of the entire secretion machine. These studies provide major insight into the structure and assembly of a broadly distributed protein secretion machine.

Graphical abstract

[#]: Correspondence: Jorge.galan@vale.edu; Jun.Liu.1@uth.tmc.edu.
[4]Co-first authors
[5]Lead Contact

SUPPLEMENTAL INFORMATION

Supplemental information includes 6 figures and 1 table and can be found with this article on line.

AUTHORS CONTRIBUTION

B. H., M. L.-T., J.L. and J. E. G. designed the studies and interpreted the results. B. H. and M. L.-T carried out the experiments. B. H., M. L.-T., J. L. and J. E. G. prepared the manuscript.

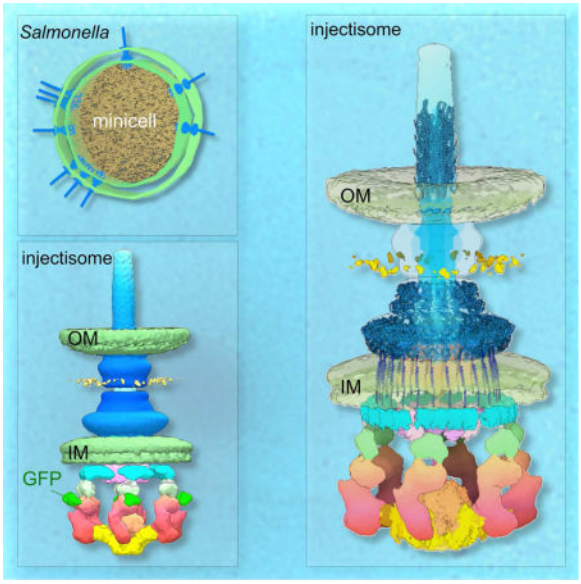

Keywords

molecular machines; protein secretion; bacterial pathogenesis; cryo electron tomography; *Salmonella* pathogenesis

INTRODUCTION

Type III protein secretion systems (T3SSs) are specialized nanomachines deployed by many bacterial species that are pathogenic to or symbiotic with vertebrates, plants, or insects (Cornelis, 2010; Galán et al., 2014). They are essential virulence factors for many important human pathogens such as *Salmonella* spp., *Shigella* spp., *Pseudomonas, Escherichia coli, Chlamydia* spp. and *Yersinia* spp. Therefore, these systems are quickly emerging as prime targets for the development of new-generation anti-infective drugs (Charro and Mota, 2015; Gu et al., 2015; Tsou et al., 2016). The type III secretion machine (or injectisome) is a complex multi-protein assembly composed of an envelope-embedded structure known as the needle complex (NC) (Kubori et al., 1998), an inner membrane export apparatus (Wagner et al., 2010), and a cytoplasmic platform that energizes the secretion process and selects and sorts substrates for their orderly delivery to the secretion machine (Lara-Tejero et al., 2011) (Fig. 1A and 1B). The NC is composed of a multi-ring cylindrical base ~26 nm in diameter that is anchored to the bacterial envelope, and a needle-like structure that projects ~60 nm from the bacterial surface (Kubori et al., 1998; Marlovits et al., 2004). The entire structure is traversed by a channel ~20 Å in diameter that serves as a conduit for the passage of proteins traveling the type III secretion pathway (Radics et al., 2013). Because the NC can be obtained in isolation in a manner suitable for single particle cryo electron microscopy (cryo-EM) analysis, significant progress has been made towards solving its atomic structure (Burkinshaw and Strynadka, 2014; Chatterjee et al., 2013; Erhardt et al., 2010; Kosarewicz et al., 2012 ; Marlovits et al., 2006; Marlovits et al., 2004; Schraidt et al., 2010; Schraidt and Marlovits, 2011). However, much less information is available regarding its intact structure

in situ. The two inner rings (IR1 and IR2) of the base substructure of the NC are composed of two proteins, which in the case of the *Salmonella* type III secretion NC are PrgH and PrgK (Kubori et al., 1998). The outer rings and the neck are made up of a single outer-membrane protein, InvG (Schraidt et al., 2010). The needle itself is made up of a single protein, PrgI, which is arranged in a helical fashion (Cordes et al., 2003; Galkin et al., 2010; Kubori et al., 2000; Loquet et al., 2012) and is connected to the base through the inner rod, also made up of a single protein (PrgJ) (Marlovits et al., 2006). The organization of the cytoplasmic platform is poorly understood because it disassociates from the NC after purification and therefore is not accessible to single particle cryo-EM analysis (Lara-Tejero et al., 2011). Recent cryo electron tomography (cryo-ET) studies have been able to visualize this structure in various pathogens (Hu et al., 2015; Kawamoto et al., 2013b; Kudryashev et al., 2013; Makino et al., 2016; Nans et al., 2015). In *Shigella* the cytoplasmic sorting platform appears as a six-pod structure, which is capped at one end by a central hub (Hu et al., 2015). This structure appears distinct from the evolutionarily related flagellar cytoplasmic C-ring structure (Thomas et al., 2001). Despite these advancements, however, the molecular organization of the cytoplasmic sorting platform remains unknown. In this study, we have used a multidisciplinary approach including a high-throughput cryo-ET pipeline and a genetically tractable bacterial minicell system to visualize *in situ* at high resolution the type III secretion nanomachine of *Salmonella enterica* serovar Typhimurium (*S.* Typhimurium) encoded within its pathogenicity island 1 (SPI-1). This study provides an unprecedented view of this highly conserved nanomachine as deployed in the bacterial envelope leading to unique insight into its structure and assembly that may aid in the development of novel therapeutic strategies to combat important infectious diseases.

RESULTS

High resolution *in situ* structure of the entire type III protein secretion machine revealed by cryo-ET

Salmonella cells are too large for high-resolution cryo-ET imaging. Therefore we made use of *S.* Typhimurium Δ*minD* mutant strains, which have a cell division defect that leads to the production of achromosomal minicells ~300 nm in diameter (Lutkenhaus, 2007). Furthermore, we utilized a protocol that maximizes partitioning of large number of functional type III secretion machines into the minicells (Carleton et al., 2013) thus enabling the implementation of high-resolution cryo-ET analysis. We first imaged frozen-hydrated minicells obtained from a minicell-producing strain of *S.* Typhimurium expressing a wild-type T3SS (Fig. 1C and 1D and Fig. S1). Our high-throughput cryo-ET pipeline effectively integrates dose-fractionation in a direct detector device with specific software, allowing massive data collection, drift correction, fiducial model generation, alignment, contrast transfer function (CTF) correction, and reconstruction of several thousands of frozen-hydrated minicells at high magnification (Morado et al., 2016). A typical three-dimensional (3D) reconstruction of a *Salmonella* minicell revealed multiple injectisomes embedded in the cell envelope (Fig. 1D and Video S1). To determine the *in situ* structure of the entire *Salmonella* type III secretion machine at high resolution, we subjected the wild-type injectisomes to sub-tomogram averaging and classification. Over 5,000 injectisome sub-tomograms (400 × 400 × 400 voxels) extracted from 1,470 tomographic reconstructions

yielded an *in situ* structure at an unprecedented level of resolution (17 Å) (Fig. 1E–1J and Fig. S1). The structure showed the membrane-embedded NC, as well as densities corresponding to the outer-membrane, peptidoglycan and inner membrane, thus providing an accurate location of the different NC elements relative to the bacterial envelope components (Fig. 1E and F). Noticeably, the structure of the intact injectisome *in situ* is significantly larger and more complex (68 nm in length × 36 nm in width, without the needle portion) than the isolated NC (32 nm in length × 26 nm in width) (Fig. 1E–1J).

The structure of the NC *in situ* closely aligned with the quasi-atomic structure of the isolated NC obtained by single particle cryo-EM (Fig. 2A–2D). The dimensions and organization of the outer ring, neck, and inner rings of these structures are virtually identical. Both the two dimensional (2D) schematic and 3D structure of the purified NC fit well into the intact injectisome maps (Fig. 2A–2D). Interestingly, in the aligned structures, the outer ring 1 (OR1) is inserted into the inner leaflet of the outer membrane and it is not long enough to reach the outer leaflet of the outer membrane resulting in an “inward pinch” to accommodate the NC structure (Fig. 1E, 1F, 2C and 2D). As a result, the outer membrane appears to “pinch inwardly”. The inner ring (IR) 1, which is predicted to be located in the periplasmic space, appears to be identical in the isolated NC and intact injectisome as shown by the close fit of the two structures in this region (Fig. 2B–2D). The IR2 in both structures formed by the cytoplasmic domain of PrgH, however, do not overlap. The superposition of the NC structure obtained from isolated particles onto the *in situ* injectisome structure would place IR2 within the inner membrane (Fig. 2B), a location not compatible with the topology of PrgH. Rather, the IR2 in the *in situ* structure is seen within the cytoplasm as predicted by the topology of PrgH (Fig. 2A–2D). These results indicate that after isolation of the NC structure and removal of the bacterial membrane, the IR2 “springs” into closer proximity to the IR1 resulting in the conformation observed in the semiatomic structure of isolated NCs (Schraidt and Marlovits, 2011). Overall, however, other than the conformational changes observed in IR2, the NC does not seem to undergo significant stretching in the bacterial envelope and we did not observe substantial heterogeneity in the dimensions of NCs observed *in situ* as previously suggested for the *Yersinia enterocolitica* injectisome (Kudryashev et al., 2013).

Molecular architecture of the export apparatus in the intact T3SS machine

Immediately beneath the center of the cytoplasmic side of the NC lies the export apparatus, which in *S.* Typhimurium is made up of the inner membrane proteins SpaP, SpaQ, SpaR, SpaS, and InvA (Wagner et al., 2010). Four of these proteins (SpaP, SpaQ, SpaR, SpaS) are thought to form the entrance to the secretion channel and provide a conduit for the type III secreted proteins to traverse the bacterial inner membrane. Furthermore, an additional inner membrane protein, InvA, is thought to be more loosely associated with the NC and is believed to perform specialized functions related to the preparation of the type III secretion substrates for secretion (Abrusci et al., 2013; Wagner et al., 2010). Comparison of the injectisome structure from *Salmonella* wild type (Fig. 3A) with those from mutants lacking InvA (Fig. 3B) or simultaneously lacking SpaP/SpaQ/SpaR/SpaS (Fig. 3C) identified specific densities associated with these components of the export apparatus. SpaP, SpaQ, SpaR, and SpaS form a funnelshaped structure that connects the needle substructure on its

wider end and the inner membrane on its narrower side (Fig. 3A and 3E). Notably, the inner membrane itself appears bent and a fenestration is apparent at its point of contact with the export apparatus (Fig. 3A). Notably, this fenestration is not apparent in mutants lacking the export apparatus components (Fig. 3C) suggesting that the deployment of these membrane proteins results in significant local reorganization of the inner membrane. InvA has a large cytoplasmic domain that has been correlated with the presence of a toroidal shape density immediately below the IR2 of the NC (Abrusci et al., 2013; Hu et al., 2015). We have confirmed this correlation by comparing the average structures from wild type and a mutant strain lacking InvA (Fig. 3B). However, the location of an individual component of a multi-protein complex is often affected by the presence or absence of other components, which makes the interpretation of this type of correlations challenging. Therefore, we sought to confirm the location of InvA by an alternative approach. The resolution afforded by single particle cryo-EM has allowed the precise localization of the individual components of multi-protein complexes by adding traceable densities to the protein of interest (Ciferri et al., 2012; Ciferri et al., 2015). This approach has been more challenging to implement in cryo-ET studies due to the relatively poor resolution and the usually small size of tags compatible with protein function (Chang et al., 2016). However, the high-resolution structural details in our average maps coupled with the predictable rigidity of the type III secretion machine prompted us to attempt to identify the position of InvA by adding a tractable protein density. We identified a region of InvA that could be tagged with a protein without altering its function (Fig. S2). To avoid potential artifacts related to over-expression, we placed the gene encoding the protein-tagged InvA within its natural chromosomal context. Comparison of the protein densities in injectisome structures derived from this strain and those of wild type identified a new density corresponding to the added tag at the bottom of the toroidal-shape density thus confirming the localization and orientation of InvA within this structure (Fig. 3D–3G and Fig. S3). Furthermore, since the tag was placed at the carboxy-terminus, the location of the extra density provided additional insight into the precise orientation of InvA within this density and a more accurate placement of its modeled atomic structure (Fig. 3F and 3G and Fig. S3). Taken together, this analysis provides major insight into the *in situ* localization of the T3SS export apparatus.

Structural characterization of the cytoplasmic sorting platform

The cytoplasmic sorting platform is a very large multi-protein complex that lies on the cytoplasmic side of the NC and it is composed of a six-pod structure 23 nm in height and 36 nm in width (Fig. 1E–1J). The overall organization of this structure closely resembles an equivalent lower resolution structure previously observed in *Shigella* (Hu et al., 2015) (Fig. S4), which is in keeping with the high degree of conservation of its components across T3SSs. However, the type III secretion sorting platform differs significantly from a related structure in the flagellar apparatus known as the “C ring”, which forms a contiguous ring beneath the flagellar basal body (Francis et al., 1994; Kawamoto et al., 2013a) (Fig. S4). The large cytoplasmic complex was observable in the absence of the export apparatus (Fig. 3B and 3C), suggesting that the formation of the large sorting platform is independent of the export apparatus. The pods are linked on their cytoplasmic-facing side by a six-spoke wheel-like structure with a central nave-like hub 12 nm in diameter, thus enclosing a chamber-like space where most likely substrates are engaged and unfolded prior to their targeting to the

export apparatus (Fig. 1E–1J). Similar features were previously observed in the *Shigella* type III secretion system (Hu et al., 2015).

In *Salmonella* the sorting platform is made up of five proteins, SpaO, OrgA, OrgB, InvI, and the hexameric ATPase InvC (Lara-Tejero et al., 2011). The sorting platform was absent in structures obtained from single gene deletion mutants in Δ*orgA*, Δ*orgB*, or Δ*spaO* (Fig. 4A–C) indicating that removal of any of these components prevents the assembly of this structure. The export apparatus appears to be intact in these mutants as supported by the presence of the toroidal shape density corresponding to InvA and the channel in the inner membrane corresponding to SpaP/SpaQ/SpaR/SpaS (Fig. 4A–C and 4F), indicating that the sorting platform is not required for the assembly of the export apparatus. The structural roles of the two additional components of the sorting platform, InvI and InvC, appear to be different from those of OrgA, OrgB, and SpaO. The absence of InvC affected the overall stability of the sorting platform as shown by the reduced density associated with this structure in the Δ*invC* mutant (Fig. 4D). However, the sorting platform was visible in this mutant and its appearance was similar to wild type except for the obvious absence of the density presumably associated with InvC (Fig. 4D and 4F). The absence of InvI had a very minor effect on the overall structure of the sorting platform (Fig. 4E and 4F).

Although previous studies have attempted to assign specific densities to individual proteins by comparing the average structures of different mutant strains lacking specific components of the sorting platform (Hu et al., 2015), it is clear that this is not an adequate strategy as removal of most of its individual component prevents the assembly of the entire sorting platform. We therefore utilized the approach described above to localize InvA and protein-tagged the different sorting platform components in a manner that did not affect their functionality and expressed them from their natural chromosomal context (Fig. S2). By comparing injectisome structures obtained from bacterial strains expressing protein-tagged versions of the different sorting platform components with that of wild type we were able to determine the precise location and orientation of all of the components of the sorting platform (Fig. 4G–4R, Fig. S5A and S5B, and Video S2). OrgA is located in the NC-most-proximal region of the pods, presumably serving as a “link” between the pods and the IR2 of the NC base (Fig. 4G and 4M). OrgB could be mapped to the hexameric spokes, which link each of the pods to the central nave of the wheel-like structure that caps the sorting platform on its cytoplasmic side (Fig. 4H and 4N). We found that as predicted by its postulated central role in the assembly of the sorting platform (Lara-Tejero et al., 2011), SpaO most likely makes up the bulk of the central segment of the pods with its amino-terminus oriented towards the NC and its carboxy-terminus merging with the spokes of the wheel-like structure (Fig. 4I and 4O). InvC was located within the hexameric nave of the wheel with its carboxy-terminus facing the toroidal-shape structure formed by the cytoplasmic domain of InvA (Fig. 4J and 4P). This observation has functional implications as the predicted substrate-binding domain of this highly conserved ATPase has been mapped to its carboxy-terminus (Akeda and Galan, 2004). InvC has been shown to unfold and remove the type III secretion substrates from their cognate chaperones prior to their initiation into the secretion pathway (Akeda and Galan, 2005). In this context, the proximal location of the substrate-binding domain of InvC to the nonameric cytoplasmic ring domain of InvA is relevant as this export apparatus component is thought to play a central role in the initiation of type III

secretion substrates into the secretion channel (Abrusci et al., 2013). InvI was located between InvC and the export apparatus component InvA (Fig. 4K and 4Q) supporting a role for this protein in the functional interplay between InvC and InvA. Sub-tomograms of a Δ*invC* mutant showed that the hexameric wheel that links the sorting platform pods retains a portion of the central nave indicating that this substructure is not entirely made of InvC (Fig. 4D). This observation indicates that OrgB must be able to engage in multiple interactions, which in addition to InvC and SpaO, must also involve other OrgB molecules at different spokes. These observations are entirely consistent with available biochemical data that has detected interactions of OrgB with itself as well as with InvC and SpaO (Diepold et al., 2010; Jackson and Plano, 2000; Lara-Tejero et al., 2011; Spaeth et al., 2009). Although the determining the precise boundaries between the different components will require the availability of atomic structures, these results provide a detailed molecular architecture of the sorting platform and have significant implications for the understanding of the mechanism of action of this essential component of the type III secretion injectisome.

Assembly of the sorting platform results in a significant remodeling of the cytoplasmic ring of the needle complex

The inner rings of the *S.* Typhimurium NC are formed by 24 copies of PrgH and PrgK, which are arranged in a concentrical fashion (Schraidt et al., 2010). Since the sorting platform is predicted to be linked to the NC through interactions with this ring structure, there must be a mechanism to adjust the disparity between the 24-fold symmetry of the NC rings and the 6-fold symmetry of the sorting platform. PrgH has a transmembrane region that separates two soluble domains, a periplasmic, well-ordered domain that forms the bulk of the IR1 and envelopes PrgK, and a more flexible domain predicted to be localized in the cytoplasm (Schraidt et al., 2010). The highresolution cryo-EM map of isolated NCs shows this domain as a ring-like extension (IR2) emanating from the transmembrane segment of PrgH (Schraidt and Marlovits, 2011). We hypothesized that this domain may function as a symmetry adaptor to link the sorting platform to the NC. To explore this hypothesis we introduced a protein tag at the amino-terminus of PrgH, which resulted in a functional protein (Fig. S2), and examined its location by cryo-ET. Analysis of sub-tomograms obtained from this strain showed the presence of an extra density in close proximity to the predicted location of the amino-terminal cytoplasmic domain of PrgH (Fig. S5C–S5F), thus confirming that the amino-terminus of PrgH is located in the cytoplasm linking the NC to the sorting platform. Surprisingly, however, sections of the sub-tomogram averages of wild type injectisomes at the level of the cytoplasmic domain of PrgH showed that rather than organized as a solid ring, as observed in isolated NCs, this domain of PrgH appeared as six discrete patches arranged in circular fashion and in close apposition to each one of the pods of the sorting platform (Fig. 5A–5E). Importantly, in the absence of the sorting platform, the patches were no longer visible and the amino-terminal domain of PrgH appeared as a solid ring comparable to its organization in isolated NCs (Fig. 5F–5J). These observations indicate that the docking of the sorting platform results in a conformational rearrangement of the cytoplasmic domain of PrgH to accommodate the 6-pod architecture of the sorting platform (Fig. S6 and Video S3).

DISCUSSION

The type III protein secretion system is a multi-protein nanomachine that is the result of a remarkable exaptation from the evolutionary related flagellar apparatus (Pallen et al., 2005). The *S.* Typhimurium T3SS encoded within its pathogenicity island 1 is made up of 15 structural proteins that organize in defined substructures that, combined, span all compartments of the bacterial cell. Early studies identified one of these substructures, the envelope-associated needle complex (Kubori et al., 1998). Because this substructure can be isolated in a manner suitable for single particle cryo EM analysis, quasi-atomic details of its organization are available (Burkinshaw and Strynadka, 2014; Chatterjee et al., 2013; Erhardt et al., 2010; Kosarewicz et al., 2012 ; Marlovits et al., 2006; Marlovits et al., 2004; Schraidt et al., 2010; Schraidt and Marlovits, 2011). However, due the limited information on its *in situ* structure, it was unclear to what extent the isolated needle complex reflected its organization when assembled in the bacterial envelope. Here we have described significant differences between the isolated and *in situ* structures of the needle complex. Although we found that the outer rings, neck and IR1 were virtually identical in both structures, we detected very significant differences in the positioning of the IR2 relative to other structural elements of the NC. While in the isolated NC the IR2 is in close apposition to the IR1, in the *in situ* structure these two rings are ~10 nm apart resulting in the IR1 located in the periplasm and the IR2 in the cytoplasm of the bacterial cell separated by the inner membrane. The structural flexibility observed in the IR2 may have functional implications not only for the assembly of the injectisome (see below) but also for the mechanisms of reprogramming of the type III secretion machine, which undergoes substrate switching during its assembly and subsequent protein delivery activity (Galán et al., 2014; Marlovits et al., 2004). Overall, however, other than the conformational changes observed in the IR2, the NC does not seem to undergo significant stretching in the bacterial envelope as has been previously suggested for the *Yersinia enterocolitica* injectisome (Kudryashev et al., 2013). Furthermore, we did not observe substantial heterogeneity in the dimensions of NCs observed *in situ*, which is also different from what has been reported for the *Yersinia* injectisomes (Kudryashev et al., 2013) but in keeping with what has been previously reported for the *Shigella* injectisome (Hu et al., 2015). It is possible that these discrepancies may be due to intrinsic differences between the NCs of these different bacteria. However other factors may account for the variance such as differences in the resolution achieved in the different studies.

Unlike the NC, very little structural information was available for the export apparatus and the cytoplasmic sorting platform because these substructures are lost during purification of the NC. We have been able to correlate the presence of the export apparatus components SpaP, SpaQ, SpaR, and SpaS with a funnel-shaped structure that connects the needle at its wider end and the inner membrane at its narrower side, which appears to undergo significant remodeling upon insertion of these membrane proteins. The presence of InvA, another export apparatus component, has been previously correlated with the presence of a toroidal shape density immediately below the IR2 of the NC (Abrusci et al., 2013) (Hu et al., 2015). By adding a tractable protein tag we were able to determine that this toroidal shape

corresponds to the large cytoplasmic domain of InvA, which could be docked into this density as a nonameric ring.

Previous studies have visualized structural elements of the sorting platform defining its general architecture (Hu et al., 2015). Similarly, we have observed that in *Salmonella* the sorting platform organizes in a cage-like manner, bounded by six pods that are capped at the cytoplasmic side by a six-pod wheel-like structure with a central prominent nave. The high resolution achieved in this study, however, has provided an unprecedented view of this injectisome substructure and has allowed us to assign the different components of the sorting platform to specific protein densities in the *in-situ* structure of the injectisome, providing an unprecedented high-resolution view of the molecular architecture of this central element of the T3SS. As predicted from previous biochemical experiments (Lara-Tejero et al., 2011), SpaO serves as a core component of the sorting platform, which is linked to the cytoplasmic inner ring of the needle complex by OrgA. We found that the spokes of the wheel that caps the sorting platform in its cytoplasmic end are made up of OrgB, which serves as a "cradle" for the ATPase InvC.

We have located the carboxy-terminus of InvC at the export apparatus-proximal side of this hexameric ATPase, which has implications for the function of the T3SS-associated ATPases. InvC has been shown to bind the effector-chaperone complexes resulting in the removal of the chaperone and the subsequent unfolding of the effectors prior to their initiation into the secretion pathway (Akeda and Galan, 2005). Although *in vitro* studies have provided evidence for these activities, many mechanistic aspects are still poorly understood. The chaperone-binding domain of InvC has been previously mapped to its carboxy-terminus (Akeda and Galan, 2004), thus the close proximity of this domain to the export apparatus suggests that removal of the chaperone and initiation of the effector proteins into the secretion pathway may be coupled. It is not clear how these ATPases exert their unfolding and chaperone-stripping functions. An appealing model is that the type III secretion associated ATPases, like some AAA+ ATPases, may unfold substrates by "threading them" through the center of the hexameric channel (Akeda and Galan, 2005). This model, however, would demand that the substrate-engaging carboxy-terminal face of the hexameric ATPase ring face the bacterial cytoplasm. However, the mapping of the location of carboxy-terminal domain of InvC on the opposite side and in close proximity to the export-apparatus suggest an alternative model for the function of InvC, not involving the threading of the substrates through the central channel.

The location of the sorting platform indicates that it must dock to the NC through interactions with its cytoplasmic ring. Consequently, the six-fold symmetry we observed in the architecture of the sorting platform presented an apparent mismatch with the 24-fold symmetry observed in the high-resolution structure of the isolated NC. However, we found that the cytoplasmic IR2 of the NC undergoes a significant conformational change upon the docking of the sorting platform resulting in its reorganization from a 24-ring structure into six equally spaced patches that align with each one of the pods of the sorting platform. The ability of the cytoplasmic domain of PrgH to undergo this significant reorganization is in keeping with the demonstrated flexibility of this domain and its observed inability to oligomerize in solution (McDowell et al., 2011). How the docking of the sorting platform

triggers this conformational rearrangement is not clear but it is likely to be driven by OrgA, which our studies have placed at the NC-most-proximal region of the sorting platform pods.

The high-resolution protein density map obtained in our studies coupled with the modeling of the available atomic structures into the cryo-ET structure (Fig. 6 and Supplementary Video S2) has allowed us to obtain an unprecedented high-resolution view of the *Salmonella* T3SS machine *in situ.* Given the high degree of conservation of type III secretion systems, these findings are likely to be relevant for the understanding of equivalent systems in other pathogens and thus could help in the development of novel anti-infective drugs.

STAR* Methods

Contact for Reagents and Resource Sharing

Contact for reagents and resource sharing should be directed to Dr. Jorge Galan (iorge.galan@yale.edu) and Dr. Jun Liu (Jun.Liu.1@uth.tmc.edu).

Experimental Model and Subject details

Bacterial strains and plasmids—All bacterial strains used in this study are derived from *Salmonella enterica* serovar Typhimurium strain SL1344 (Hoiseth and Stocker, 1981) and are listed in resource Table. All strains were constructed by standard recombinant DNA and allelic exchange procedures as previously described (Kaniga et al., 1994).

Method Details

Analysis of type III protein secretion function—The functionality of the type III secretion system in the different *S.* Typhimurium strains was carried out by examining their ability to secrete type III secreted proteins to the culture supernatant. Briefly, overnight cultures of the specific strains were diluted 1/20 into LB containing 0.3M NaCl to induce the expression of SPI-1 T3SS (Galán and Curtiss III, 1990). Diluted cultures were grown at 37°C on a rotating wheel to an OD600 of ~ 0.9 (4 to 5 hours) and then the cells were pelleted by centrifugation at 6,000 rpm. The cell pellet was resuspended in 1X SDS-running buffer at 10X concentration so that 10 μl of the resuspension equaled 100 μl of cells. The culture supernatants were filtered through a 0.45 μm syringe filter and proteins in the supernatant were recovered by trichloroacetic acid (TCA) precipitation. The protein precipitate was resuspended in 1x SDS-running buffer at 100X concentration so that 10 μl of the resuspension equaled 1 ml of culture supernatant. Ten μl of whole cell lysate sample (100 μl of cells) and 10 μl of supernatant sample (1 ml of supernatant) were run on a 10% SDS-PAGE gel for Western blot analysis with antibodies against the type III secreted proteins SipB, SipC and InvJ.

Preparation of Frozen-Hydrated Specimens—Bacterial cultures were grown overnight at 37 °C in LB containing 0.3M NaCl and fresh cultures were prepared from a 1:100 dilution and then grown at 37 °C to late log phase in the presence of ampicillin (200 μg/mL) and L-arabinose (0.1%) to induce the expression of regulatory protein HilA and thus increase the number of injectisomes partitioning to the minicells (Carleton et al., 2013). To enrich for minicells, the culture was centrifuged at 1,000 × g for 5 min to remove bacterial

cells, and the supernatant fraction was further centrifuged at 20,000 × g for 20 min to collect the minicells. The minicell-enriched preparations were then mixed with 10 nm colloidal gold particles (used as fiducial markers in image alignment) and then deposited onto freshly glow-discharged, holey carbon grids for 1 min. The grids were blotted with filter paper and rapidly frozen in liquid ethane, using a gravity-driven plunger apparatus as described previously(Hu et al., 2015).

Cryo-ET Data Collection and 3D Reconstructions—The frozen-hydrated specimens were imaged at −170 °C using a Polara G2 electron microscope (FEI Company) equipped with a field emission gun and a direct detection device (Gatan K2 Summit). The microscope was operated at 300 kV with a magnification of ×15,500, resulting in an effective pixel size of 2.6 Å at the specimen level. We used SerialEM (Mastronarde, 2005) to collect low-dose, single-axis tilt series with dose fractionation mode at about 5 μm defocus and a cumulative dose of ~50 $e^{-}/Å^{2}$ distributed over 35 stacks covering an angular range of −51° to +51° with 3° fixed increments. Each stack contains ~8 images. To analyze over 60 TB raw data from the microscope and the direct detection device, we used Tomoauto (Morado et al., 2016) to facilitate image processing: drift correction of dose-fractionated data using Motioncorr (Li et al., 2013) assembly of corrected sums into tilt series, automatic fiducial seed model generation, alignment, defocus estimation, and contrast transfer function correction of tilt series using IMOD (Kremer et al., 1996), and weighted back projection (WBP) reconstruction of tilt series into tomograms using Tomo3D (Agulleiro and Fernandez, 2015). Each tomographic reconstruction is 3,710 × 3,838 × 1,800 voxels and ~100Gb in size. In total, 5,592 tomographic reconstructions (about 600 TB data) from 17 different strains were successfully generated and were then utilized for the subsequent sub-tomogram analysis (Table S1). The original WBP tomograms were too noisy for direct visualization of cellular features. Therefore, we also used Tomo3D (Agulleiro and Fernandez, 2015) to generate high contrast tomograms (618 × 639 × 300 voxels) from the binned by 6 aligned tilt series by simultaneous iterative reconstruction technique (SIRT). Some representative snapshots of the SIRT reconstructions from 16 strains are shown in Fig. S1.

Sub-tomogram averaging and correspondence analysis—We used tomographic package I3 (Winkler, 2007) for sub-tomogram analysis as described previously (Hu et al., 2015). A total of 29,307 sub-tomograms of the injectisomes (400 × 400 × 400 voxels) were visually identified in the SIRT reconstructions and then extracted from 5,592 the WBP reconstructions (3,710 × 3,838 × 1,800 voxels) of the minicells. Two of the three Euler angles of each injectisome were estimated based on the orientation of each particle in the cell envelope. To accelerate image analysis, 4 × 4 × 4 binned sub-tomograms (100 × 100 × 100 voxels) were used for initial alignment and classification. The alignment proceeded iteratively with each iteration consisting of three parts in which references and classification masks are generated, sub-tomograms are aligned and classified, and finally class averages are aligned to each other. Class averages showed similar structural features: the bacterial envelope-associated needle complex, the inner membrane export apparatus, and the large cytoplasmic sorting platform. After multiple cycles of alignment and classification for 4 × 4 × 4 binned subtomograms, we used original unpinned sub-tomograms for refinement. Fourier shell correlation (FSC) between the two independent reconstructions was used to

estimate the resolution of the averaged structures (Fig. S1). The final maps have been deposited in the Electron Microscopy Data Bank (EMDB) with accession codes EMD-8544 and EMD-8545.

3D Visualization and Molecular Modeling—We used IMOD to visualize the maps and to generate 3D surface rendering of *Salmonella* minicells and UCSF Chimera (Pettersen et al., 2004) (http://www.rbvi.ucsf.edu/chimera) to visualize sub-tomogram averages in 3D and molecular modeling. To better visualize the tag densities, we used the difference maps between the injectisome structure with specific tags and the wild type injectisome structure, and then used UCSF Chimera for segmentation and surface rendering. The EM map of the purified NC from *Salmonella* (EMD-1875) was fitted into our intact injectisome map using the function "fit in map" in UCSF Chimera (Pettersen et al., 2004). We built the initial model based on the following refined structures from *S.* Typhimurium: $InvG_N$ (the amino-terminal domain of InvG: PDB-3J1V) (Bergeron et al., 2013), $PrgH_C$ (the carboxyterminal domain of PrgH: PDB-3J1X) (Bergeron et al., 2013), and $PrgH_N$ (the amino-terminal domain of PrgH: PDB-3J1W) (Bergeron et al., 2013). A large remodeling was required to refine $PrgH_C$. $InvA_C$ (the carboxy-terminal domain of InvA: PDB-2×4a) (Worrall et al., 2010) was used to build the nonameric ring based on the homologous structure from *Shigella flexneri* $MxiA_C$ (PDB-4A5P) (Abrusci et al., 2013). Structures of the flagellar ATPase complex FliI–FliH (PDB-5B0O) (Imada et al., 2016) and FliJ (PDB-3AJW) (Ibuki et al., 2011) were used to build the model of the InvC–InvI–OrgB complex.

Modeling of the InvA nonameric ring: We built the $InvA_C$ nonameric ring using the $MxiA_C$ nonameric ring as a template (Fig. S3), and then we fitted the modeled structure into our intact injectisome map using the function "fit in map" in UCSF Chimera. Comparison of the protein densities in sub-tomograms of minicells obtained from the wild type strain with those obtained from a strain expressing a GFP-tagged InvA identified a new density at the bottom of the toroidal-shape density corresponding to the protein tag confirming the localization of InvA within this structure (Fig. 3 and Fig. S3). Furthermore, since the GFP tag was placed at the carboxy-terminus of InvA, the location of the extra density confirms the orientation of the $InvA_C$ nonameric ring, which guided the placement of the atomic structure into the cryo-ET map (Fig. S3).

Modeling of InvG, PrgK and PrgH: The protein density map of the purified *S.* Typhimurium NC (EMD-1875) (Schraidt and Marlovits, 2011) was fitted into our intact injectisome map using the function "fit in map" in UCSF Chimera. The major structural scaffold of the NC base is comprised of 15 copies of InvG, which form the neck and outer rings, and 24 copies each of PrgH and PrgK, which are arranged in a concentric fashion and form the inner rings. Secondary structure prediction analysis indicates that PrgH contains a transmembrane domain (from amino acid 142 to 162), which separates the protein into two soluble domains, the amino-terminal domain located in the cytoplasm and the carboxy-terminal domain located in the periplasm (Fig. S6). We built the initial model of the NC base using the map of the purified *S.* Typhimurium NC (EMD-1875), and the atomic structures of InvG (PDB-3J1V), the carboxy-terminal domain of PrgH (PDB-3J1X), and the amino-termimal domain of PrgH (PDB-3J1W) (Bergeron et al., 2013).

Modeling of InvC and OrgB: Comparison of tomograms obtained from a *S.* Typhimurium Δ*invC* mutant with those of wild type identified a missing density located within the central nave-like hub that connects the six spokes of the wheel-like structure that caps the sorting platform on the cytoplasmic side (Fig. 4). This density most likely corresponds to InvC. To confirm the location and orientation of InvC, we imaged a *S.* Typhimurium strain expressing InvC tagged at its carboxy-terminus by GFP, which when compared with wild type showed an additional density (presumably corresponding to the GFP tag) on the membrane-facing side of nave-like hub. This observation suggests that the carboxy-terminus of InvC faces the export apparatus components such as the carboxy-terminus of InvA (Fig. 4). In the flagellar ATPase complex, $FliH_{C2}$ (a homolog of OrgB) shows an unusually asymmetric homodimeric structure that binds to the amino-terminal region of the ATPase FliI (a homolog of InvC) (Imada et al., 2016). A hexameric ring model of the $FliH_{C2}$-FliI complex has been built previously using the hexamer model of V-type ATPase as a template (Imada et al., 2016). Using this model as well as the partial structure of the OrgB-SpaO complex (Notti et al., 2015) we built a model in which the hexameric InvC ATPase fits the nave-like hub density we observed in our sub-tomogram averages, and the structure of $OrgB_{C2}$ fits well into the spokes of the wheel-like structure that cradles the InvC hexamer. The model places the Cterminal domain of InvC facing the export apparatus, and the carboxy-sand amino-terminal domains of OrgB interacting with InvC and SpaO, respectively. The model provides further support to the proposed location of OrgB and InvC.

Modeling of InvI: InvI is a small coiled-coil protein similar to the F1-γ subunit and flagellar protein FliJ (Ibuki et al., 2011). FliJ binds in the central pore of the $FliI_6$ ring (the homolog of InvC) to form the $FliI_6FliJ$ complex, which resembles the F1-α3β3γ complex. To gain insight into the potential location of InvI we compared sub-tomogram averages obtained from a strain that expresses InvI tagged at its amino-terminus by GFP with those of wild type. After density subtraction we detected an additional density, presumably corresponding to GFP, located at the center of the export-apparatus-facing side of the proposed InvC hexameric ring.

Quantification and Statistical Analysis

Quantification and statistical analyses are integral parts of the algorithms and software used in our high throughput cryo-electron tomography pipeline. In particular, massive data enabled us to use multivariate statistical analysis and classification (which are implemented in tomographic package i3) for processing and interpretation of the sub-tomograms of injectisomes extracted from *Salmonella* minicell reconstructions.

Data and Software Availability

All software used in this study have been extensively described in previous publications from our and other laboratories. See the Methods Details section for citations to the original publications. All data are available upon request. The final sub-tomogram averages have been deposited in the Electron Microscopy Data Bank (EMDB) with the accession codes EMD-8544 and EMD-8545.

Supplementary Material

Refer to Web version on PubMed Central for supplementary material.

Acknowledgments

We thank members of the Galán laboratory for critical reading of the manuscript. This work was supported by Grants AI030492 (to J. E. G.) and AI112680 (to Q. K) from the National Institute of Allergy and Infectious Diseases and GM107629 from the National Institute of General Medicine (to J. L), and AU-1714 from the Welch Foundation (to J. L.).

References

Abrusci P, Vergara-Irigaray M, Johnson S, Beeby M, Hendrixon D, Roversi P, Friede M, Deane J, Jensens G, Tang C, et al. Architecture of the major component of the type III secretion system export apparatus. Nat Struct Mol Biol. 2013; 20:99–104. [PubMed: 23222644]

Agulleiro JI, Fernandez JJ. Tomo3D 2.0–exploitation of advanced vector extensions (AVX) for 3D reconstruction. J Struct Biol. 2015; 189:147–152. [PubMed: 25528570]

Akeda Y, Galan JE. Genetic analysis of the Salmonella enterica type III secretion-associated ATPase InvC defines discrete functional domains. J Bacteriol. 2004; 186:2402–2412. [PubMed: 15060043]

Akeda Y, Galan JE. Chaperone release and unfolding of substrates in type III secretion. Nature. 2005; 437:911–915. [PubMed: 16208377]

Bergeron JR, Worrall LJ, Sgourakis NG, Dimaio F, Pfuetzner RA, Felise HB, Vuckovic M, Yu AC, Miller SI, Baker D, et al. A Refined Model of the Prototypical Salmonella SPI-1 T3SS Basal Body Reveals the Molecular Basis for Its Assembly. Plos Pathog. 2013; 9:e1003307. [PubMed: 23633951]

Burkinshaw B, Strynadka N. Assembly and structure of the T3SS. Biochim Biophys Acta. 2014; 1843:1649–1663. [PubMed: 24512838]

Carleton HA, Lara-Tejero M, Liu X, E GJ. Engineering the type III secretion system in non-replicating bacterial minicells for antigen delivery. Nature Commun. 2013; 4:1590–1596. [PubMed: 23481398]

Chang Y, Rettberg L, Treuner-Lange A, Iwasa J, Søgaard-Andersen L, Jensen G. Architecture of the type IVa pilus machine. Science. 2016; 351:aad2001. [PubMed: 26965631]

Charro N, Mota L. Approaches targeting the type III secretion system to treat or prevent bacterial infections. Expert Opin Drug Discov. 2015; 10:373–387. [PubMed: 25727140]

Chatterjee S, Battaile K, Lovell S, Plano G, De Guzman R. Structure and biophysics of type III secretion in bacteria. Biochemistry. 2013; 52:2508–2517. [PubMed: 23521714]

Ciferri C, Lander G, Maiolica A, Herzog F, Aebersold R, Nogales E. Molecular architecture of human polycomb repressive complex Elife. 2012; 1:e00005. [PubMed: 23110252]

Ciferri C, Lander G, Nogales E. Protein domain mapping by internal labeling and single particle electron microscopy. J Struct Biol. 2015; 192:159–162. [PubMed: 26431894]

Cordes FS, Komoriya K, Larquet E, Yang S, Egelman EH, Blocker A, Lea SM. Helical structure of the needle of the type III secretion system of Shigella flexneri. J Biol Chem. 2003

Cornelis G. The type III secretion injectisome, a complex nanomachine for intracellular ‘toxin’ delivery. Biol Chem. 2010; 391:745–751. [PubMed: 20482311]

Diepold A, Amstutz M, Abel S, Sorg I, Jenal U, Cornelis G. Deciphering the assembly of the Yersinia type III secretion injectisome. EMBO J. 2010; 29:1928–1940. [PubMed: 20453832]

Erhardt M, Namba K, Hughes K. Bacterial nanomachines: the flagellum and type III injectisome. Cold Spring Harb perspect Biol. 2010; 2:a000299. [PubMed: 20926516]

Francis N, Sosinsky G, Thomas D, DeRosier D. Isolation, characterization and structure of bacterial flagellar motors containing the switch complex. J Mol Biol. 1994; 235:1261–1270. [PubMed: 8308888]

Galán J, Lara-Tejero M, Marlovits T, Wagner S. Bacterial type III secretion systems: specialized nanomachines for protein delivery into target cells. Annu Rev Microbiol. 2014; 68:415–438. [PubMed: 25002086]

Galán JE, Curtiss R III. Expression of *Salmonella typhimurium* genes required for invasion is regulated by changes in DNA supercoiling. Infect Immun. 1990; 58:1879–1885. [PubMed: 2160435]

Galkin V, Schmied W, Schriadt O, Marlovits T, Egelman E. The structure of the Salmonella typhimurium type III secretion system needle shows divergence from the flagellar system. J Mol Biol. 2010; 396:1392–1397. [PubMed: 20060835]

Gu L, Zhou S, Zhu L, Liang C, Chen X. Small-Molecule Inhibitors of the Type III Secretion System. Molecules. 2015; 20:17659–17674. [PubMed: 26404233]

Hoiseth SK, Stocker BA. Aromatic-dependent *Salmonella typhimurium* are non-virulent and effective as live vaccines. Nature. 1981; 291:238–239. [PubMed: 7015147]

Hu B, Morado D, Margolin W, Rohde J, Arizmendi O, Picking W, Picking W, Liu J. Visualization of the type III secretion sorting platform of Shigella flexneri. Proc Natl Acad Sci U S A. 2015; 112:1047–1052. [PubMed: 25583506]

Ibuki T, Imada K, Minamino T, Kato T, Miyata T, Namba K. Common architecture of the flagellar type III protein export apparatus and F-and V-type ATPases. NatStructMolBiol. 2011; 18:277–282.

Imada K, Minamino T, Uchida Y, Kinoshita M, Namba K. Insight into the flagella type III export revealed by the complex structure of the type III ATPase and its regulator. ProcNatlAcadSciUSA. 2016; 113:3633–3638.

Jackson M, Plano G. Interactions between type III secretion apparatus components from Yersinia pestis detected using the yeast two-hybrid system. FEMS Microbiol Lett. 2000; 186:85–90. [PubMed: 10779717]

Kaniga K, Bossio JC, Galan JE. The Salmonella typhimurium invasion genes invF and invG encode homologues of the AraC and PulD family of proteins. Mol Microbiol. 1994; 13:555–568. [PubMed: 7997169]

Kawamoto A, Morimoto Y, Miyata T, Minamino T, Hughes K, Kato T, Namba K. Common and distinct structural featues of Salmonella injectisome and flagellar basal body. Sci Rep. 2013a; 3:3369. [PubMed: 24284544]

Kawamoto A, Morimoto Y, Miyata T, Minamino T, Hughes K, Kato T, Namba K. Common and distinct structural features of Salmonella injectisome and flagellar basal body. Sci Rep. 2013b; 3(3369):3369–3376. [PubMed: 24284544]

Kosarewicz A, Königsmaier L, Marlovits T. The blueprint of the type-3 injectisome. Philos Trans R Soc Lond B Biol Sci. 2012; 367:1140–1154. [PubMed: 22411984]

Kremer J, Mastronarde D, McIntosh J. Computer visualization of threedimensional image data using IMOD. J Struct Biol. 1996; 116:71–76. [PubMed: 8742726]

Kubori T, Matsushima Y, Nakamura D, Uralil J, Lara-Tejero M, Sukhan A, Galán JE, Aizawa SI. Supramolecular structure of the *Salmonella typhimurium* type III protein secretion system. Science. 1998; 280:602–605. [PubMed: 9554854]

Kubori T, Sukhan A, Aizawa SI, Galan JE. Molecular characterization and assembly of the needle complex of the Salmonella typhimurium type III protein secretion system. Proc Natl Acad Sci U S A. 2000; 97:10225–10230. [PubMed: 10944190]

Kudryashev M, Stenta M, Schmelz S, Amstutz M, Wiesand U, Castaõ-Diaz D, Degiacomi M, Munnich S, Bleck C, Kowal J, et al. In situ structural analysis of the Yersinia enterocolitica injectisome. eLife. 2013; 2:e00792. [PubMed: 23908767]

Lara-Tejero M, Kato J, Wagner S, Liu X, Galan JE. A sorting platform determines the order of protein secretion in bacterial type III systems. Science. 2011; 331:1188–1191. [PubMed: 21292939]

Li X, Mooney P, Zheng S, Booth C, Braunfeld M, Gubbens S, Agard D, Cheng Y. Electron counting and beam-induced motion correction enable near-atomicresolution single-particle cryo-EM. Nature Methods. 2013; 10:584–590. [PubMed: 23644547]

Loquet A, Sgourakis N, Gupta R, Giller K, Riedel D, Goosmann C, Griesinger C, Kolbe M, Baker D, Becker S, et al. Atomic model of the type III secretion system needle. Nature. 2012; 486:276–279. [PubMed: 22699623]

Lutkenhaus J. Assembly dynamics of the bacterial MinCDE system and spatial regulation of the Z ring. Annu Rev Biochem. 2007; 76:539–562. [PubMed: 17328675]

Makino F, Shen D, Kajimura N, Kawamoto A, Pissaridou P, Oswin H, Pain M, Murillo I, Namba K, Blocker A. The Architecture of the Cytoplasmic Region of Type III Secretion Systems. Sci Rep. 2016; 6:33341. [PubMed: 27686865]

Marlovits TC, Kubori T, Lara-Tejero M, Thomas D, Unger VM, Galan JE. Assembly of the inner rod determines needle length in the type III secretion injectisome. Nature. 2006; 441:637–640. [PubMed: 16738660]

Marlovits TC, Kubori T, Sukhan A, Thomas DR, Galan JE, Unger VM. Structural insights into the assembly of the type III secretion needle complex. Science. 2004; 306:1040–1042. [PubMed: 15528446]

Mastronarde D. Automated electron microscope tomography using robust prediction of specimen movements. J Struct Biol. 2005; 152:36–51. [PubMed: 16182563]

McDowell M, Johnson S, Deane J, Cheung M, Roehrich A, Blocker A, McDonnell J, Lea S. Structural and Functional Studies on the N-terminal Domain of the Shigella Type III Secretion Protein MxiG. J Biol Chem. 2011; 286:30606–30614. [PubMed: 21733840]

Morado D, Hu B, Liu J. Using Tomoauto: A Protocol for High-throughput Automated Cryo-electron Tomography. J Vis Exp. 2016; 107:e53608.

Nans A, Kudryashev M, Saibil H, Hayward R. Structure of a bacterial type III secretion system in contact with a host membrane in situ. Nat Commun. 2015; 6:10114. [PubMed: 26656452]

Notti R, Bhattacharya S, Lilic M, Stebbins C. A common assembly module in injectisome and flagellar type III secretion sorting platforms. Nat Commun. 2015; 6:7125–7133. [PubMed: 25994170]

Pallen M, Beatson S, Bailey C. Bioinformatics, genomics and evolution of nonflagellar type-III secretion systems: a Darwinian perspective. FEMS Microbiol Rev. 2005; 29:201–229. [PubMed: 15808742]

Pettersen EF, Goddard TD, Huang CC, Couch GS, Greenblatt DM, Meng EC, Ferrin TE. UCSF Chimera–a visualization system for exploratory research and analysis. J Comput Chem. 2004; 25:1605–1612. [PubMed: 15264254]

Radics J, Konigsmaier L, Marlovits T. Structure of a pathogenic type 3 secretion system in action. Nat Struct Mol Biol. 2013

Schraidt O, Lefebre M, Brunner M, Schmied W, Schmidt A, Radics J, Mechtler K, Galan J, Marlovits T. Topology and organization of the Salmonella typhimurium type III secretion needle complex components. PLoS Pathog. 2010; 6:e1000824. [PubMed: 20368966]

Schraidt O, Marlovits T. Three-dimensional model of Salmonella's needle complex at subnanometer resolution. Science. 2011; 331:1192–1195. [PubMed: 21385715]

Spaeth K, Chen Y, Valdivia R. The Chlamydia type III secretion system C-ring engages a chaperone-effector protein complex. PLoS Pathog. 2009; 5:e1000579. [PubMed: 19750218]

Thomas D, Morgan D, DeRosier D. Structures of bacterial flagellar motors from two FliF-FliG gene fusion mutants. J Bacteriol. 2001; 183:6404–6412. [PubMed: 11591685]

Tsou L, Lara-Tejero M, RoseFigura J, Zhang Z, Wang Y, Yount J, Lefebre M, Dossa P, Kato J, Guan F, et al. Antibacterial Flavonoids from Medicinal Plants Covalently Inactivate Type III Protein Secretion Substrates. J Am Chem Soc. 2016; 138:2209–2218. [PubMed: 26847396]

Wagner S, Königsmaier L, Lara-Tejero M, Lefebre M, Marlovits T, Galán J. Organization and coordinated assembly of the type III secretion export apparatus. Proc Natl Acad Sci USA. 2010; 107:17745–17750. [PubMed: 20876096]

Winkler H. 3D reconstruction and processing of volumetric data in cryo-electron tomography. J Struct Biol. 2007; 157:126–137. [PubMed: 16973379]

Worrall L, Vuckovic M, Strynadka N. Crystal structure of the C-terminal domain of the Salmonella type III secretion system export apparatus protein InvA. Protein Sci. 2010; 19:1091–1096. [PubMed: 20306492]

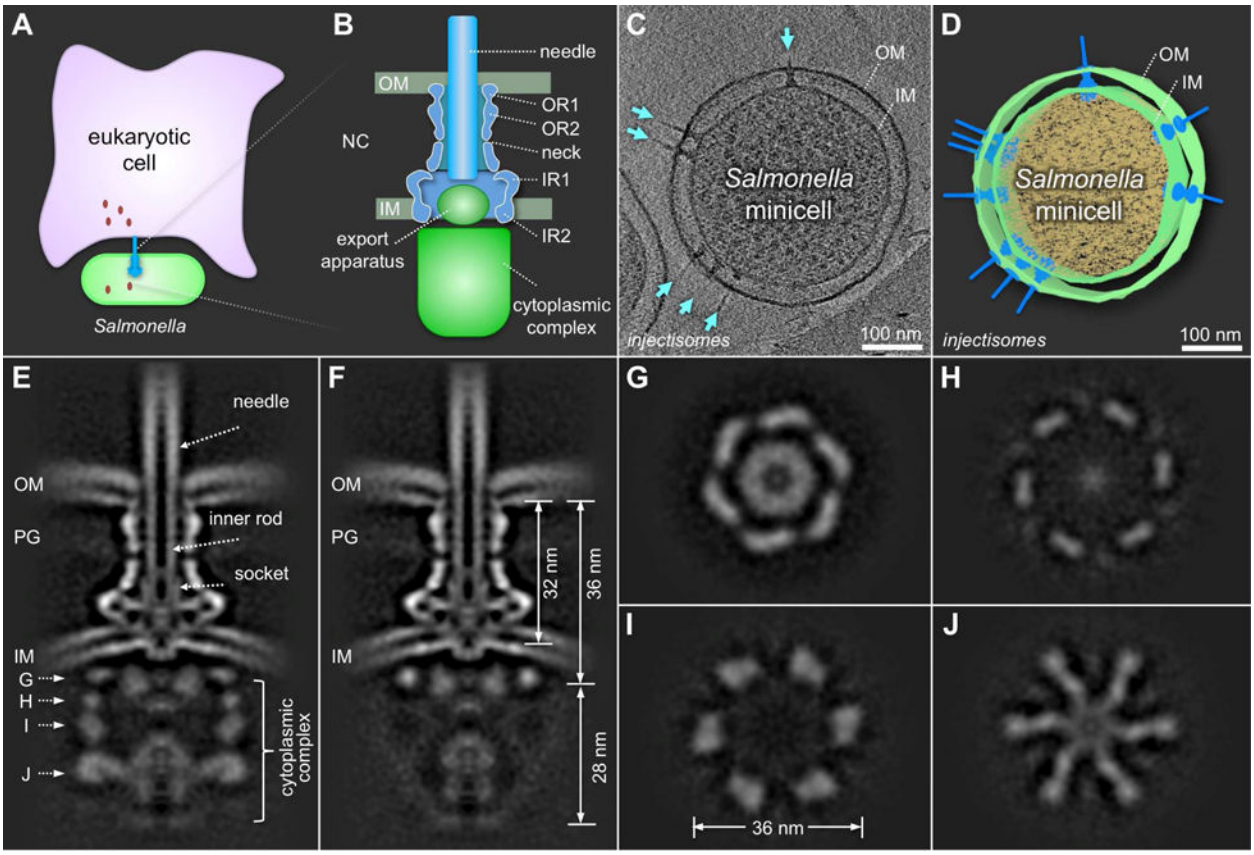

Figure 1. High resolution *in situ* structure of the entire type III protein secretion machine revealed by cryo-ET

(**A**) A schematic diagram of *Salmonella* delivering effector proteins into a target cell via a T3SS machine. (**B**) A schematic representation of the intact T3SS machine. (**C**) and (**D**) A tomographic slice (**C**) and a 3-D surface view (**D**) from a representative *Salmonella* minicell showing multiple injectisomes embedded in the cell envelope. (**E** and **F**) Central sections through different planes of the cytoplasmic sorting platform of a global average structure of the intact T3SS injectisome *in situ* show the components of the T3SS injectisome in the context of the outer membrane (OM), the peptidoglycan (PG), and the inner membrane (IM). (**G–J**) Cross-sections at the positions indicated in panel (**E**), are shown. See also Fig. S1, S4, and Table S1.

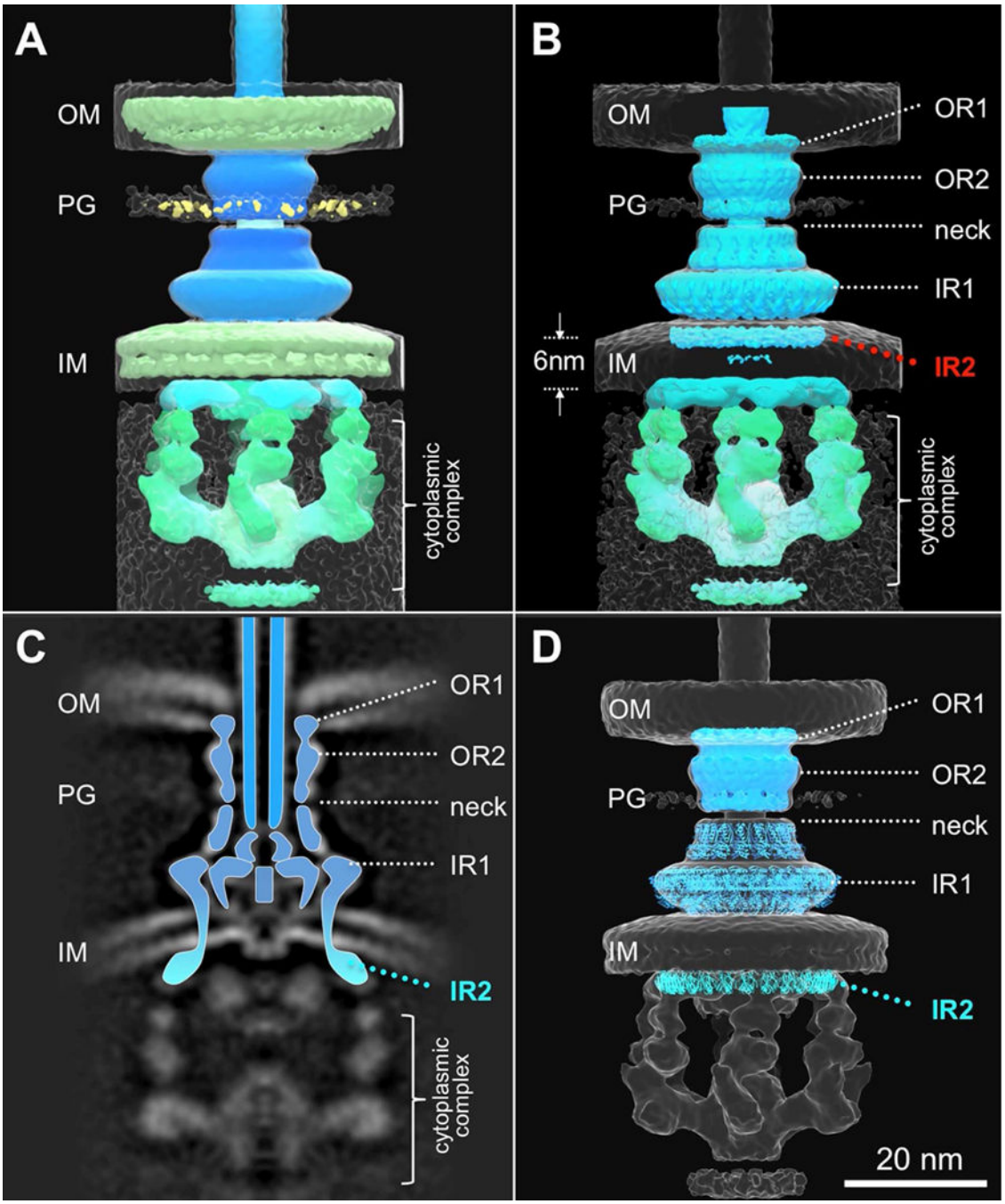

Figure 2. Comparison of the *in situ* and isolated structures of the type III secretion needle complex

(A) 3-D surface rendering of the intact injectisome structure shown in two different contour levels. Part of the map (colored in blue) matches well with the isolated NC structure. The rest of the map (green) can only be seen *in situ.* (**B**) 3D view of the superposition of the isolated NC protein density map (EMD-1875) onto the *in situ* injectisome structure. While the two structures match well in the central section (OR1, OR2 neck and IR1), a large shift of the IR2 is required to place it at its proper location in the cytoplasmic side of the inner

membrane (IM) (**C**). The IR2 is placed within the inner membrane (**B**), to highlight a position that would be incompatible with the topology of the membrane protein components. (**D**) The atomic models of InvG and PrgH fit well into the 3D map of the intact injectisome *in situ* structure. See also Fig. S4 and Table S1.

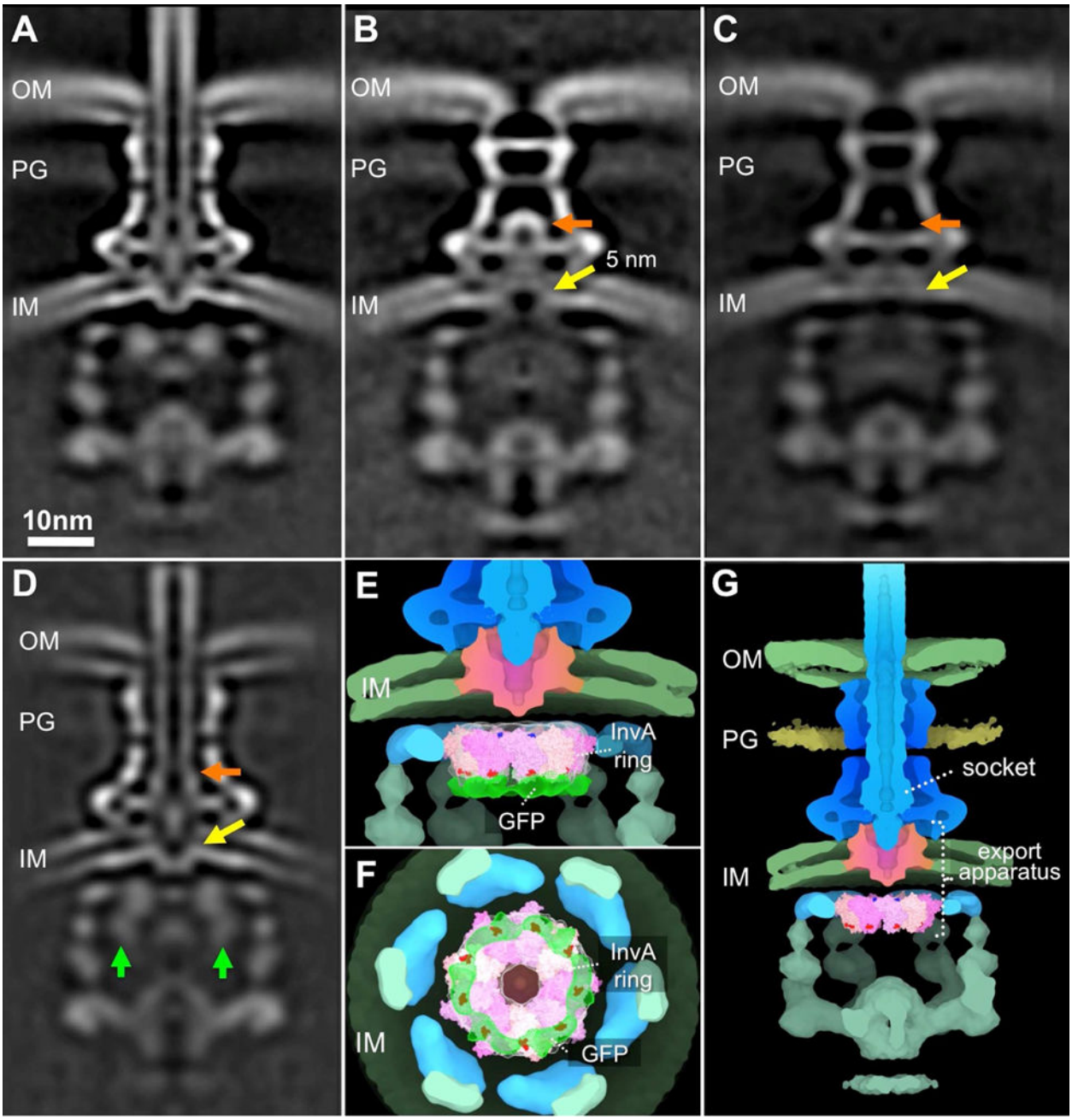

Figure 3. Molecular architecture of the export apparatus in the intact T3SS machine

(A and **B)** A central section of the sub-tomogram average of the injectisome structure in wild type (**A**) and a Δ*invA* deletion mutant (**B**). A large portion of the cytoplasmic complex remains, while a toroidal shape density immediately below the inner ring of the NC is absent. It appears that there is a ~5 nm fenestration (yellow arrow) in the inner leaflet of the inner membrane (**B**). (**C)** A central section of the sub-tomogram average of injectisomes from a quadruple deletion mutant lacking *spaP, spaQ, spaR*, and *spaS.* The toroidal shape density, the socket (orange arrow) and the needle fail to assemble, while a large portion of the cytopasmic complex remains intact. The fenestration observed at the inner membrane (**B**,

yellow arrow) is no longer apparent in this mutant strain. Noticeably, the two leaflets of the inner membrane appear differently in the two mutants (**B** and **C**) and the wild type (**A**). (**D**) A central section of the sub-tomogram average of injectisomes from a strain expressing GFP-tagged InvA. Additional protein densities at the bottom the toroidal shape density (green arrows) are apparent in this strain, most likely representing the GFP tag added to the carboxy-terminus of InvA. (**E–G**) The nonameric ring atomic modeled structure of the carboxy-terminus of InvA fits well into the toroidal shape density in both side (**E**) and bottom (**F**) views. The additional densities assigned to GFP are shown in green (**E** and **F**). The InvA nonameric ring in the context of the entire injectisome is shown purple and the export apparatus in pink (**G**). See also Fig. S2, S3 and Table S1.

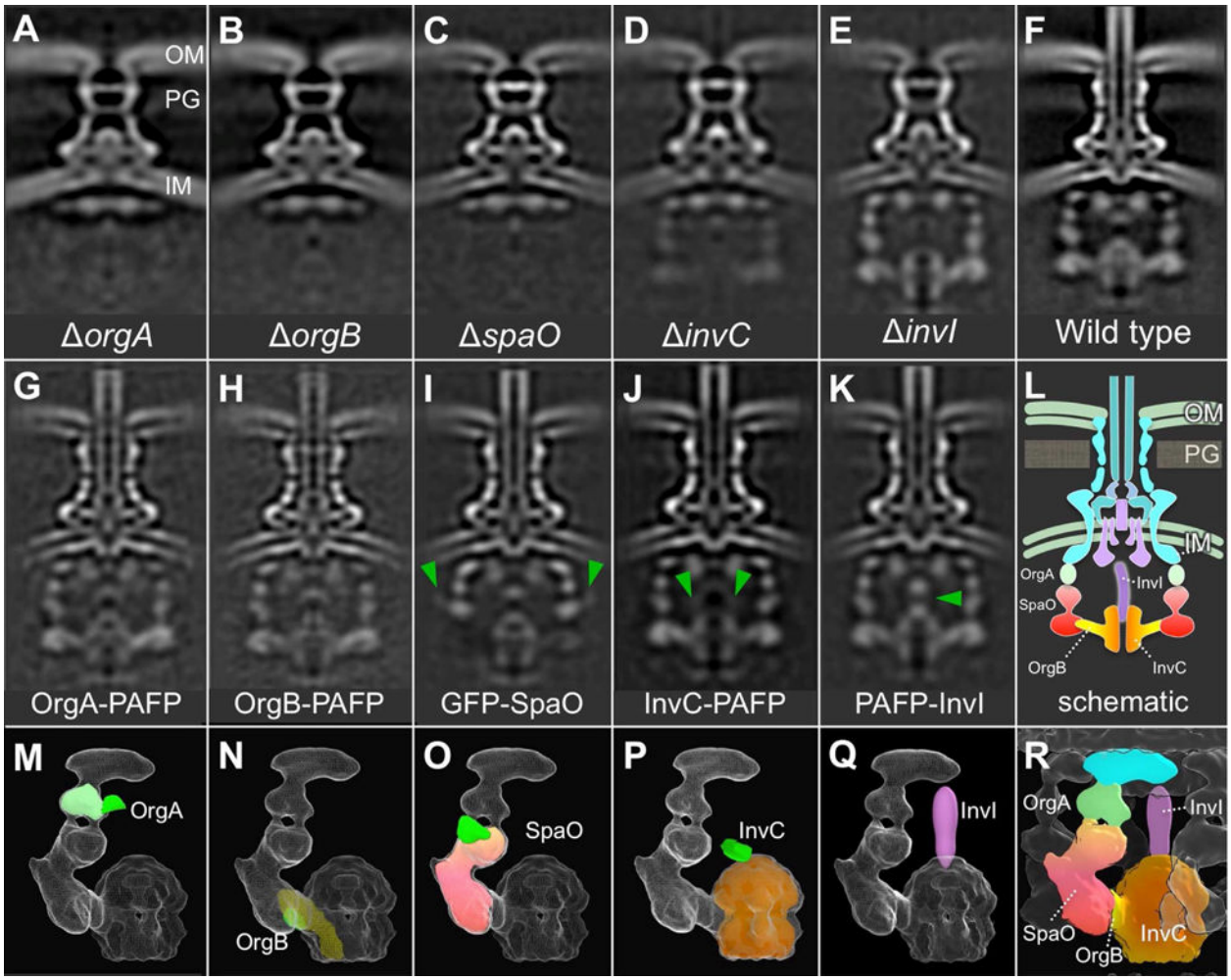

Figure 4. Structural characterization of the cytoplasmic sorting platform

Central sections of the sub-tomogram averages of injectisomes from Δ*orgA* (**A**), Δ*orgB* (**B**), Δ*spaO* (**C**), Δ*invC* (**D**), Δ*invi* (**E**), and wild type (WT) (**F**) *S.* Typhimurium strains. The export apparatus appears to be intact in these mutants (**A–E**) compared to the WT injectisome structures (**F**). Most cytoplasmic densities are absent in Δ*orgA* (**A**), Δ*orgB* (**B**), and Δ*spaO* (**C**), suggesting that these three proteins are essential for the assembly of the sorting platform. In the absence Δ*invC* (**D**), the densities associated with the sorting platform are present although substantially reduced suggesting that InvC contributes to the stability of this structure. In contrast, in the Δ*invi* mutant (**E**) the sorting platform is almost indistinguishable from wild type, suggesting a minor structural role for InvI. Central sections of the sub-tomogram averages of injectisomes obtained from strains expressing tagged versions of OrgA (**G**), OrgB (**H**), SpaO (**i**), InvC (**J**), and InvI (**K**) are shown. The location of the protein tag in the 3D rendering of the different structures is highlighted in panels as indicated (**M–Q**). A model of the proposed location of the different components of the sorting platform is shown in schematic (**L**) and 3D (**R**) manner (OrgA: green; InvC: orange; OrgB: yellow; SpaO: red; and PrgH: cyan. See also Fig. S2, S5, and Table S1.

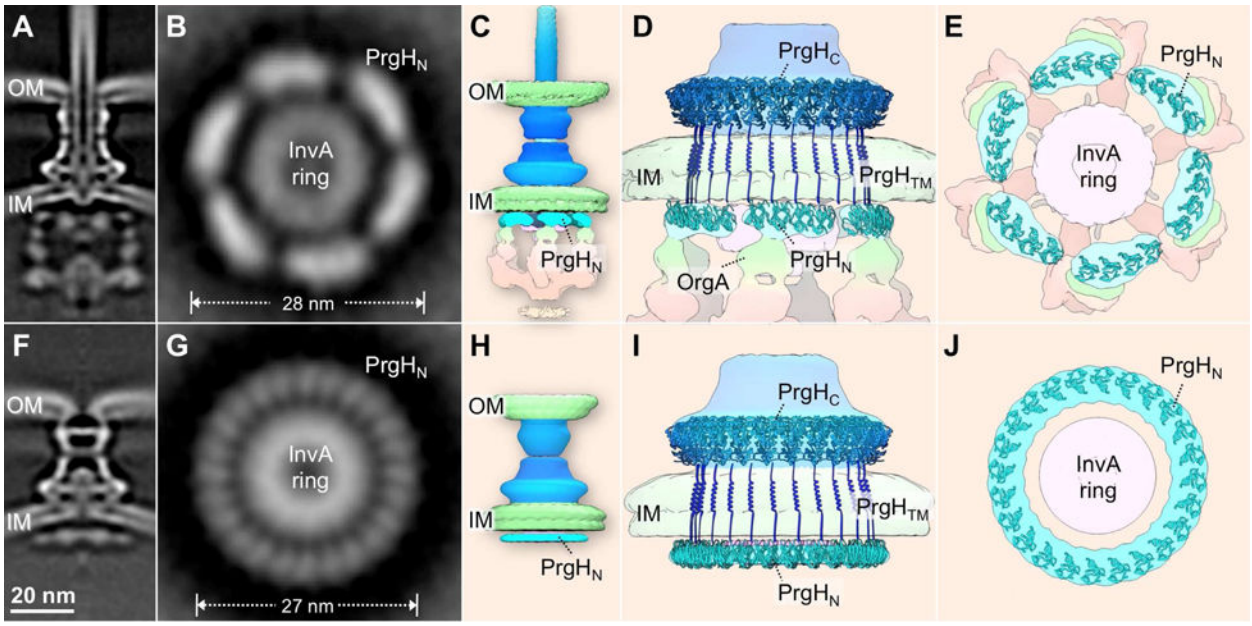

Figure 5. Remodeling of PrgH amino-terminal domain upon sorting platform assembly

Organization of the amino-terminal cytoplasmic domain of PrgH (PrgH$_N$) in the presence (**A–E**) or in the absence (**F–J**) of the sorting platform. Central (**A** and **F**) and cross (**B** and **G**) sections, or surface renderings (**C** and **H**) of the injectisomes from a *S.* Typhimurium wild type (**A–C**) or a strain lacking the sorting platform *(*Δ*orgA* Δ*orgB* Δ*spaO)* (**F–H**) depicting the densities associated with PrgH$_N$ (light blue) are shown. The fitting of the atomic structure of PrgH$_N$ into the respective wild type (**D** and **E**) or Δ*orgA* Δ*orgB* Δ*spaO* (**I** and **J**) injectisomes are shown depicting the conformational changes of PrgH$_N$ that occur upon assembly of the sorting platform. See also Fig. S5, S6, and Table S1.

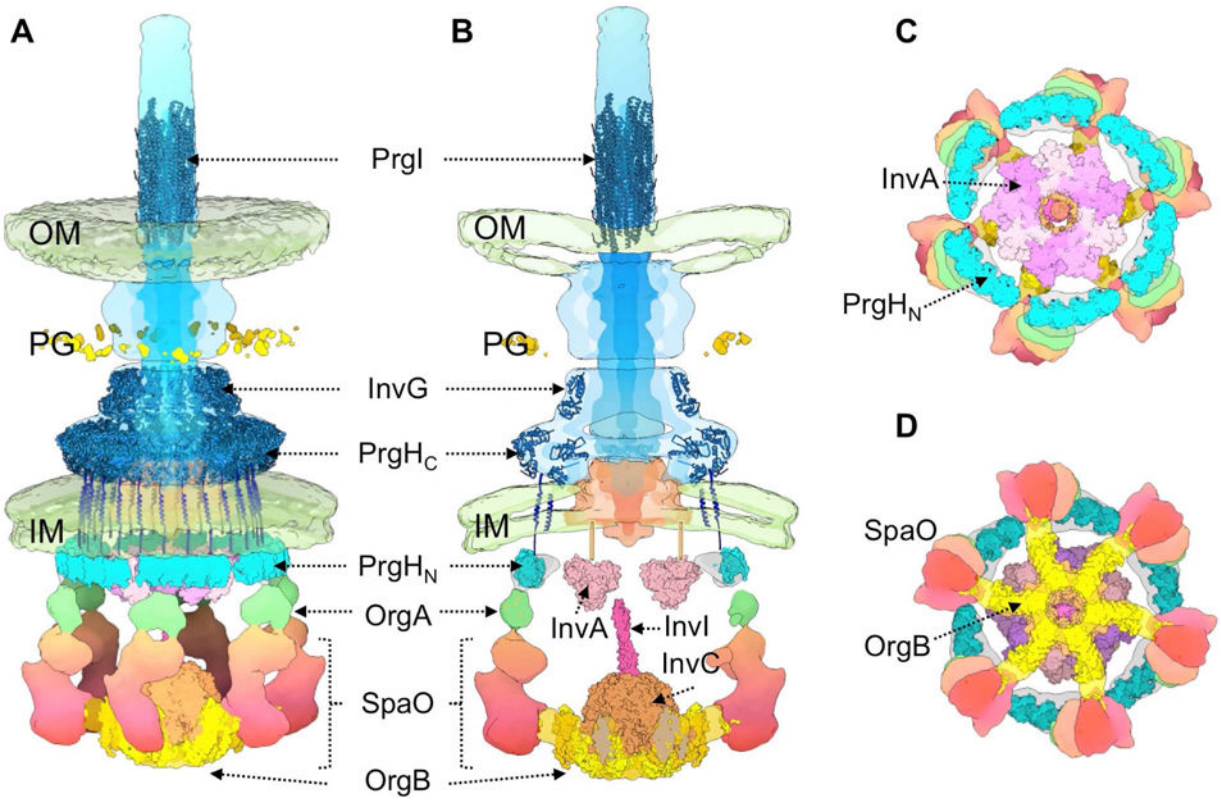

Figure 6. Molecular model of the organization of the entire T3SS machine *in situ*

Side (**A**), cut–through (**B**), top (**C**), and bottom (**D**) views the intact injectisome structure. The available (or modeled) atomic structures of $PrgH_C$, $PrgH_N$, PrgK, PrgI, $InvA_C$, OrgB, InvC and InvI have been fitted into the structure (see supplementary on line text). The location of the outer membrane (OM), inner membrane (IM), and peptidoglycan (PG) of the bacterial envelope are indicated.